# Measurement of the point-spread function of a noisy imaging system

**Christopher D. Claxton and Richard C. Staunton***

*School of Engineering, University of Warwick, Coventry, CV4 7AL, UK*
**Corresponding author: R.C.Staunton@warwick.ac.uk*

Received May 17, 2007; revised September 18, 2007; accepted October 2, 2007;
posted October 11, 2007 (Doc. ID 83145); published December 18, 2007

The averaged point-spread function (PSF) estimation of an image acquisition system is important for many computer vision applications, including edge detection and depth from defocus. The paper compares several mathematical models of the PSF and presents an improved measurement technique that enables subpixel estimation of 2D functions. New methods for noise suppression and uneven illumination modeling were incorporated. The PSF was computed from an ensemble of edge-spread function measurements. The generalized Gaussian was shown to be an 8 times better fit to the estimated PSF than the Gaussian and a 14 times better fit than the pillbox model. © 2007 Optical Society of America

*OCIS codes:* 110.2970, 110.4850, 220.4840, 350.4600, 150.5670, 220.2560.

## 1. INTRODUCTION

The research reported concerns mathematical modeling and practical measurement of the point-spread function (PSF) of focused and defocused image acquisition systems, such as digital TV cameras. This measure of image blur can be utilized to optimize image processing functions such as edge detection [1–3] and depth-from-defocus (DFD) depth estimation [4–11]. An image acquisition system typically consists of optical components (such as lenses and apertures) and electronic components (such as the 2D CCD array, antialiasing, and communication circuits). Each of the components in the optical and electronic paths can be considered as spatial low-pass filters. Considering the system in the terminology of system theory, the transfer functions of each of its components can be estimated and then all combined to find the overall transfer function. Alternatively—and the approach taken in this work—the transfer function for the entire system can be measured. Typically, input signals are provided in the form of bar patterns, point sources, or step edges. For entire system measurement, the output signal is the captured digital image.

The Fourier transform of the PSF is the optical transfer function (OTF), and both measures have been widely used to characterize systems. The lens can be thought of as a 2D low-pass filter with a spatial cutoff frequency that is limited by diffraction and aberration effects. The 2D array samples the image and also includes low-pass filtering, as the individual sensor elements have a finite area required for low light operation. Together the elements tile the image plane. As a simple model, charge generated by a photon at a point in an element will distribute evenly across the tile [12]. The sampled value is then proportional to the accumulated charge from all the photons converted in the element during the acquisition phase and since the previous sample was acquired. The CCD is read by a raster scanning process [12]. Here the charge in each of the elements is transferred to vertical columns of shift registers. In turn these shift into a horizontal register and are shifted to an analog charge-to-voltage converter and then further electronics that provide, nominally, 1D signal processes such as low-pass filtering and digitization. The low-pass filtering provided by the lens is necessary as it acts as an antialiasing filter for the image discretization. CCD elements require a relatively large area for the camera to work well at low light levels, and this finite area limits the high-frequency response.

PSF measurements can be limited by the Nyquist frequency of the discretization in the acquisition system; however, an averaging and accumulation process was researched to overcome this [2,13,14]. This process required a knife- or step-edge to be imaged; i.e., this is not a general technique for all images. The image was of a blurred step and several edge-spread functions (ESF) were estimated along the length of the edge. The ESFs were then each registered to a reference point and accumulated to form a superresolution ESF that contained frequency information above the Nyquist limit of the sampling grid. The PSF is more useful than the ESF for DFD measurement and image simulation as it can be directly convolved with an input image to estimate the output image [2,6,9]. The PSF is obtained by differentiating the ESF; however, even low levels of noise in the ESF can result in high levels of noise in the PSF and render it unusable. The source of the noise is in the imaging system's sensors and electronics. In this research it was found that both digital and inexpensive analog TV cameras had too poor a signal-to-noise ratio (SNR) for the previous PSF measurement techniques to work reliably.

In this paper we compare research into several methods to both reduce the noise in the ESF estimation and to accurately model usable PSFs for the acquisition system. In Section 2 we review PSF measurement techniques and describe how a superresolution ESF—and eventually a PSF—is computed from an ensemble of low-resolution measurements. In Section 3 we examine the theoretical

 

PSF models that result from consideration of both geometric and diffraction optics. In Section 4 we describe improvements to the traditional superresolution PSF measurement technique that involve (i) compensation for nonuniform illumination within the lightbox used to produce the test images, (ii) a regularized numerical differentiation process to limit noise in the computed PSF, and (iii) models of the ESF that have been developed and used to compute PSFs that have then been compared with the theoretical models described in Section 2. Fitting the correct ESF model to the measured data is key to obtaining accurate PSFs for the system. Section 5 presents the experimental results from both focused and defocused systems. Specific 1D results have been used to demonstrate problems with noise in the ESF estimation, and bias to the PSF when nonuniform illumination remains uncompensated. Then the results of ESF fitting experiments have been reported and discussed. Finally 2D PSF plots have been produced for the most successful fitting methods. Section 6 provides conclusions.

## 2. MEASUREMENT TECHNIQUES

Here we are proposing PSF measurement of the whole system; however, methods exist to measure individual PSFs for each component. These can then be combined to give the overall PSF. Lasers have been used to measure the PSFs of individual pixels within the CCD array [15,16]. These are a function of wavelength, and so a complete characterization is lengthy and complex. However, the PSF for the array is spatially variant and widely used in image restoration. Classically, images of sinusoidal gratings have been used for OTF lens measurements. When a focal-plane array (FPA) images the grating, the discretization means that the FPA must be moved relative to the image to give minimum and maximum modulation transfer function (MTF) curves [17]. Sinusoidal laser interference patterns have been used by Marchywka and Socker [18], and laser speckle techniques can also be employed [19]. The main limitation of lasers is the monochromatic light. Spatial domain techniques have been used to measure the PSF of a lens. A scanned point source can be used to obtain a 2D PSF containing local blur and aberration information up to the Nyquist limit of the FPA. A 2D unit intensity step, known as a knife-edge, can be easily produced experimentally using a lightbox. Differentiating the response of the lens, the ESF, gives the PSF.

The knife-edge technique can be extended to acquisition system measurement. If the system contains a FPA, then undersampling effects cause errors in the PSF estimation due to aliasing. In practice PSF information beyond the Nyquist limit of the array is often required. Reichenbach *et al.* [13] solved the problem by using many ESF profiles to create a superresolution image of a 1D edge. Tzannes and Mooney [14] fitted a sum of three Fermi–Dirac functions to the edge to reduce the noise during differentiation to obtain the PSF, and Staunton [2] extended the technique to measure the ESF for many differently angled edges to produce a 2D PSF and MTF. At edge angles other than 0 or 90°, a resampling of the data was performed to obtain the discrete ESFs along normals to the edge. A normal was set and then the samples closest to it projected onto it from a direction parallel to the edge as shown by the dashed lines in Fig. 1. The sampled values were then not equally spaced along the normal, but this was irrelevant to the following superresolution stage.

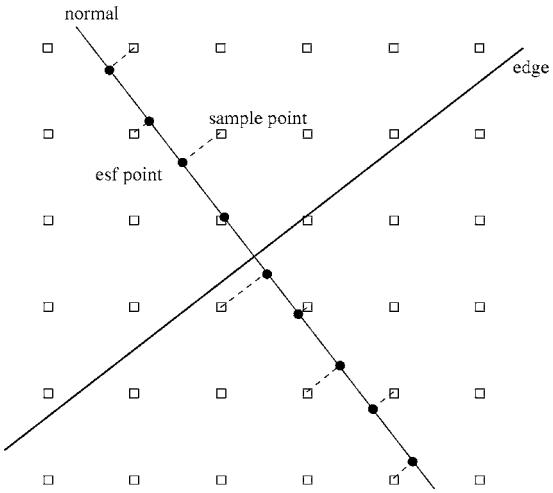

Fig. 1. Migration of samples onto the ESF.

To understand the superresolution stage used in [2,13,14], consider an edge oriented close to but not actually at 0°. The edge cuts each pixel along its length so that part of the pixel is brightly illuminated, and part is dark. The sampled value for each pixel along the edge is proportional to the averaged illumination throughout the pixel. Each sampled value along the edge is therefore different. In the same way each of the many ESFs located at the pixels along the edge comprises differently sampled values. These low-resolution ESFs are then registered with one another and assembled to form a single high-resolution ESF that is resampled onto typically a 0.1 pixel grid.

The proposed knife-edge technique is simple to perform, but the PSF measurements are averaged along the length of the edge. Such an average is advantageous for shift invariant models used in processes such as edge-detector testing [2], DFD [6], or image simulation, but may be disadvantageous for processes that require models of lens aberrations in addition to spherical aberration, such as may be required for image restoration [20]. These may require space variant estimation of the PSF.

## 3. THEORETICAL PSF MODELS

### A. Geometrical Optics

Pentland [4] showed that for the simple defocused optical system shown in Fig. 2, and assuming geometrical optics, the PSF is a pillbox shape with a blur circle radius given by

$$r = \frac{v_o u - F(v_o + u)}{2fu}, \tag{1}$$

where $v_o$ is the distance between the lens and the CCD, $u$ is the depth of the object, $F$ is the focal length of the lens, and $f$ is the $f$-number, which is defined as $f=F/d$, where $d$ is the diameter of the aperture. The distance $u_o$ is the dis-

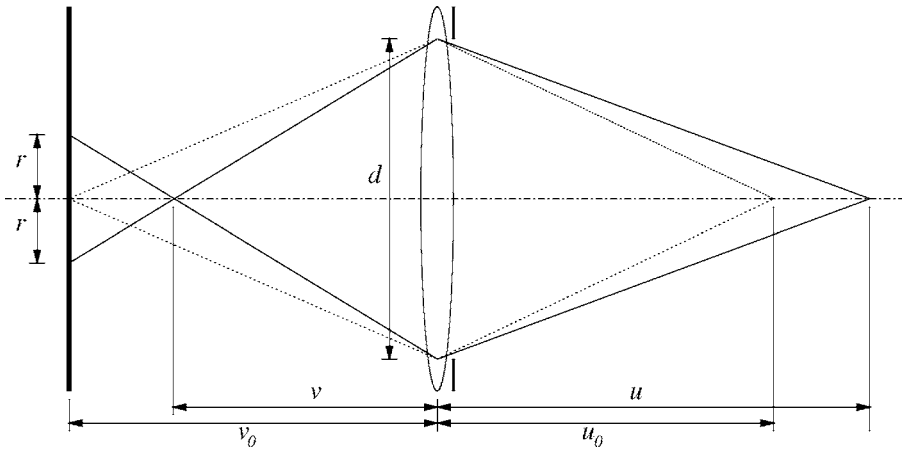


Fig. 2. Simple model of the optical system with the image plane on the left.

tance at which an object would appear in focus on the image plane.

### B. Diffraction Approach

The PSF $h(\mathbf{x})$ of a focused lens that is subject to diffraction effects and with optical aberrations as a function $\theta(\mathbf{x})$, but neglecting sampling due to the FPA, is given by [21] as

$$h(\mathbf{x}) = \left| \int A(\xi) e^{j\theta(\xi)} e^{-j2\pi\xi\mathbf{x}/\lambda F} \mathrm{d}\xi \right|^2, \tag{2}$$

where $\mathbf{x}$ is a position vector, $A(\xi)$ is the aperture function, $\lambda$ is the wavelength of light, and $F$ is the focal length of the lens. Out-of-focus blurring can be modeled as a quadratic aberration of the form

$$\theta(\mathbf{x}) = \frac{\pi}{\lambda}\left(\frac{1}{u} + \frac{1}{v} - \frac{1}{F}\right)|\mathbf{x}|^2, \tag{3}$$

where $u$ is the distance between the object and the lens, and $v$ is the distance between the FPA and the lens. By substituting Eq. (3) into Eq. (2); assuming polychromatic light with equal intensities between wavelengths $\lambda_1$ and $\lambda_2$ and assuming the aperture function $A(\xi)$ to be a circle of radius $r$, then in 1D the PSF becomes

$$h(x) = \int_{\lambda_1}^{\lambda_2} \left| \int_{-r}^{+r} e^{-j\pi/\lambda[2\xi x/F - (1/u + 1/v - 1/F)]|\xi|^2} \mathrm{d}\xi \right|^2 \mathrm{d}\lambda. \tag{4}$$

Figure 3(a) shows a PSF expected for a focused system where only diffraction is present. The polychromatic light is modeled as white light with equal intensity components in the range 400 to 700 nm. The PSF looks similar to a Gaussian. Figure 3(b) shows a PSF for a defocused 16 mm lens where the camera is focused at 0.464 m and the point source is at 0.8 m. The PSF has been flattened out and made to look more like a pillbox function.

## 4. IMPROVEMENTS TO EDGE-SPREAD FUNCTION ESTIMATION

In this research the knife-edge technique was employed and this section first considers an improvement to Staunton's algorithm [2] that incorporates the effect of nonuniform illumination of the lightbox. Without noise the ESF could be differentiated to yield the PSF, but differentiating a noisy function amplifies the noise. In this paper models of the ESF are developed from several PSF models and then compared. A regularized numerical differentiation process is proposed.

### A. Compensation for Nonuniform Illumination

An ideal brightness step changes abruptly from one constant brightness level to the other. Experimentally a lightbox was employed with a knife-edge to approximate the step; however, in practice the brightness of each region was significantly nonuniform. This resulted in erroneous PSFs. We propose a new model that retains the abrupt transition, but allows each region to have a linear change in intensity as a function of spatial position. As an

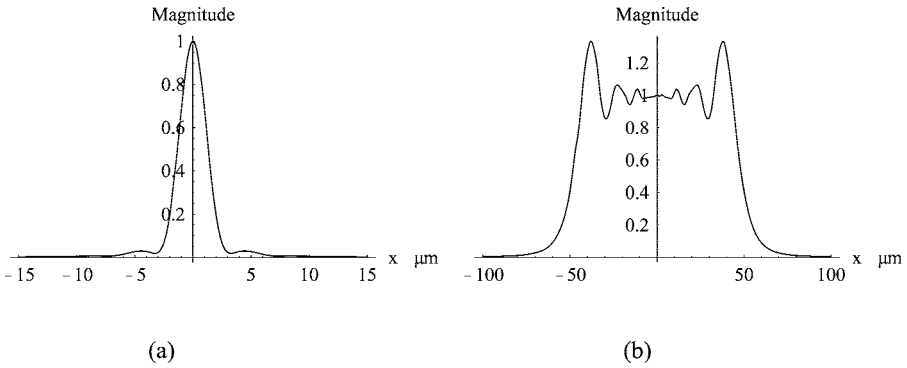


(a) (b)

Fig. 3. Normalized-magnitude PSFs for a 16 mm, $f/4$ lens: (a) focused, (b) defocused.

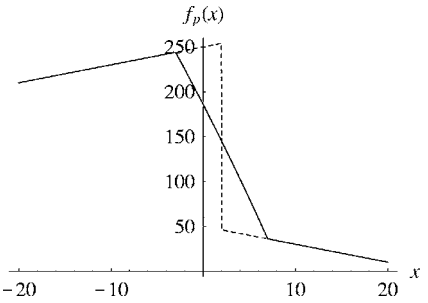


Fig. 4. ESF with a pillbox PSF where $\sigma=5$ (solid curve) and the ideal step edge (dashed curve).

example, shown by the dotted trace in Fig. 4, both the bright and darker areas of this particular lightbox increase in intensity toward the knife-edge. However other linear illumination field conditions can also be modeled by this scheme. The modified step was given by

$$s(x) = (m_1 x + c_1)u(x + x_0) + (m_2 x + c_2)u(x - x_0), \tag{5}$$

where $u(x)$ is the unit step function, $c_1$ and $c_2$ are the brightness of the upper and lower regions, and $m_1$ and $m_2$ are the gradients of the brightness.

### B. ESF Assuming a Pillbox PSF

For a defocused lens under geometrical optics the PSF is a pillbox and given by

$$h_p(x) = \frac{1}{2\sigma}[u(x + \sigma) - u(x - \sigma)], \tag{6}$$

where $\sigma$ is the radius of the pillbox, and hence the blur circle. The ESF assuming a pillbox PSF and using Eq. (5) becomes

$$g_p(x) = \begin{cases} m_1 x + c_1 & x - x_0 < -\sigma \\ \dfrac{1}{4\sigma}\{-[2c_1 + m_1(x + x_0 - \sigma)](x - x_0 - \sigma) + (x - x_0 + \sigma)[2c_2 + m_2(x + x_0 + \sigma)]\} & -\sigma \leq x - x_0 \leq \sigma, \\ m_2 x + c_2 & \sigma < x - x_0 \end{cases} \tag{7}$$

where $x_0$ is the location of the transition [22]. An example of the ESF for a PSF with a blur circle radius $\sigma=5$ is shown in Fig. 4 where the original step is shown with a dotted line.

Note that there are two sharp transitions in the resulting ESF. A pillbox PSF would result if the lens passed every spatial frequency; however, due to diffraction it is known that this is not possible and a smoother PSF will result.

### C. ESF Modeled as a Sum of Fermi–Dirac Functions

Tzannes and Mooney [14] fitted a sum of three Fermi–Dirac functions to the ESF. Their technique resulted in a smoothed transition across the edge. In general form the sum of $N$ Fermi–Dirac functions for modeling the ESF is

$$g_{FD}(x) = \sum_{i=1}^{N}\left[\frac{a_i}{1 + \exp\left(\dfrac{x - b_i}{c_i}\right)}\right] + d, \tag{8}$$

where constants $a_i$ have been added to normalize the intensity, $b_i$ to set the center point, $c_i$ to control the gradient, and $d$ to account for the nonzero brightness of the lowest level. To recover the PSF the ESF must be differentiated, which is given by [22] as

$$h_{FD}(x) = \frac{\partial g_{FD}(x)}{\partial x} = -\sum_{i=1}^{N}\left\{\frac{a_i \exp\left(\dfrac{x - b_i}{c_i}\right)}{c_i\left[1 + \exp\left(\dfrac{x - b_i}{c_i}\right)\right]^2}\right\}. \tag{9}$$

However, a problem with this model is that it cannot readily take into account the nonuniform illumination in a way that allows the step and the PSF to be separated. The PSFs determined experimentally were consequently nonsymmetrical, as shown for example in Fig. 10 below.

### D. ESF Assuming a Gaussian PSF

The Gaussian PSF is the most frequently assumed model found in the literature on defocused lenses, and this is partly because of its simplicity. A 1D Gaussian with a standard deviation $\sigma$ and centered at $x=\bar{x}$ is then given by

$$h_g(x) = \frac{1}{\sqrt{2\pi}\sigma}\exp\left[-\frac{1}{2}\frac{(x - \bar{x})^2}{\sigma^2}\right]. \tag{10}$$

The ESF assuming a Gaussian PSF and a step-edge with nonuniform illumination is given by [22] as

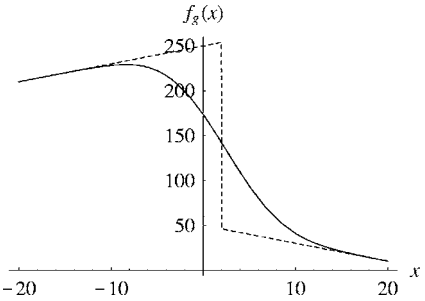


Fig. 5. ESF when the PSF is a Gaussian with $\sigma=5$ (solid curve) and unevenly illuminated ideal step edge (dashed curve).

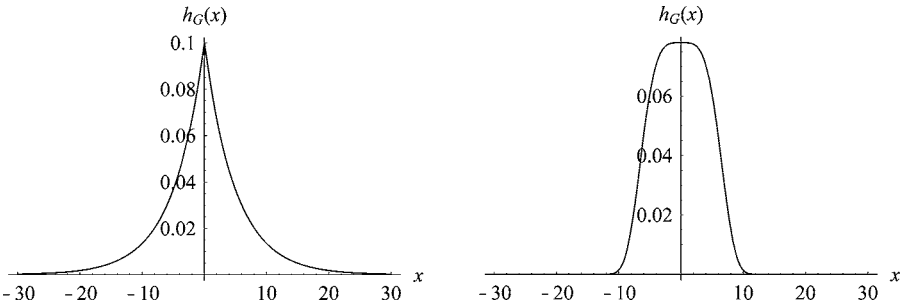


Fig. 6. Generalized Gaussian PSFs where (left) $p=1$, $\sigma=5$ and (right) $p=4$, $\sigma=5$.

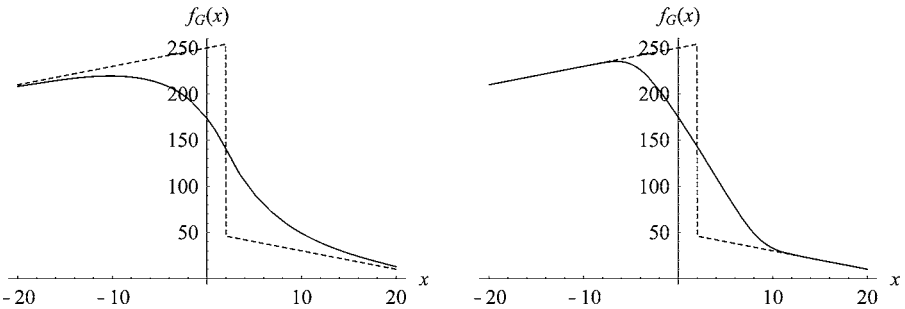


Fig. 7. Ideal steps (dashed curves) and the ESFs (solid curves) assuming generalized Gaussian PSFs with (left) $p=1$, $\sigma=5$ and (right) $p=4$, $\sigma=5$.

$$g_g(x) = \frac{1}{2}\left(-(m_1+m_2)\sigma\sqrt{\frac{2}{\sigma}}\exp\left[-\frac{(x-\bar{x})^2}{2\sigma^2}\right] + (m_1x+c_1)\left\{1-\mathrm{erf}\left[\frac{(x-\bar{x})}{\sigma\sqrt{2}}\right]\right\} + (m_2x+c_2)\left\{1-\mathrm{erf}\left[\frac{(x-\bar{x})}{\sigma\sqrt{2}}\right]\right\}\right), \tag{11}$$

where erf(·) is the error function, defined as

$$\mathrm{erf}(x) = \frac{2}{\sqrt{\pi}}\int_0^x \exp(-t^2)\mathrm{d}t. \tag{12}$$

If the ideal step with nonuniform illumination as shown in Fig. 4 is defocused with a Gaussian ($\sigma=5$, $\bar{x}=0$) then the ESF is as shown in Fig. 5.

### E. ESF Assuming a Generalized Gaussian PSF

The generalized Gaussian function [23] is being proposed here as a model of the PSF of a defocused lens. Along with the mean $\bar{x}$ and the standard deviation $\sigma$, the power $p$ of the function is required. The function can take the form of a Gaussian when the power $p=2$ and a pillbox when $p=\infty$, and thus encompasses both of the frequently used models of defocus. The generalized Gaussian is

$$h_G(x) = \frac{p^{1-1/p}}{2\sigma\Gamma\left(\frac{1}{p}\right)}\exp\left(-\frac{1}{p}\frac{|x-\bar{x}|^p}{\sigma^p}\right), \tag{13}$$

where $\Gamma(\cdot)$ is the gamma function and $|\cdot|$ represents the modulus. The term before the exponential ensures the function has unit area. Two generalized Gaussian functions are presented in Fig. 6, where $p=1$ (e.g., for a lens in focus) and $p=4$ (defocused).

The ESF, assuming a step edge with nonuniform illumination and a generalized Gaussian PSF, is given by the convolution of Eq. (11) with Eq. (13). A closed-form, algebraic solution could not be found, so the convolution integral was evaluated numerically. The ESF is given in [22] as

$$g_G(x) = \frac{p^{1-1/p}}{2\sigma\Gamma\left(\frac{1}{p}\right)}\int_{x-x_0}^{\infty}\exp\left(-\frac{1}{p}\frac{|\xi|^p}{\sigma^p}\right)[m_1(x-\xi)+c_1]\mathrm{d}\xi + \frac{p^{1-1/p}}{2\sigma\Gamma\left(\frac{1}{p}\right)}\int_{-\infty}^{x-x_0}\exp\left(-\frac{1}{p}\frac{|\xi|^p}{\sigma^p}\right)[m_2(x-\xi)+c_2]\mathrm{d}\xi. \tag{14}$$

Using the PSFs shown in Fig. 6 and the ideal step with nonuniform illumination, we obtain the ESFs shown in Fig. 7.

### F. Regularized Numerical Differentiation

To recover the PSF from the superresolution (ESF) the response must be differentiated, and as the data are discrete, finite-difference approximations must be employed. However, the ESF is noisy, and both two- and five-point numerical differentiation were found to give poor results. Chartrand [24] considered the problem of finding the derivative of a function when the underlying function is noisy and has a discontinuity in the derivative. The solution proposed uses total-variation regularization, where the derivative of a function $y(x)$ defined on the closed interval $[0,L]$ is the minimizer of the function

Fig. 8. Example of the windowed image.

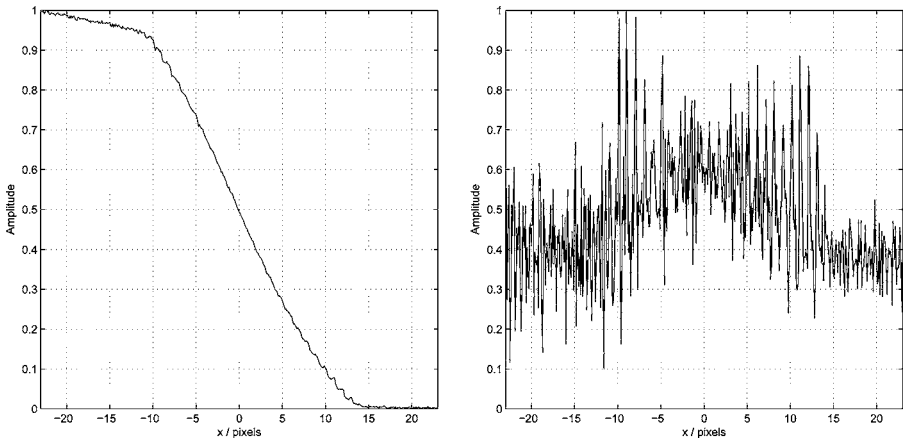


Fig. 9. Five-point numerical differentiation results for $f/2.8$, $z=0.725$ m, angle$=0°$ with ESF shown on the left and PSF on the right.

$$Y(u) = \alpha \int_0^L |u'(x)| \mathrm{d}x + \frac{1}{2} \int_0^L \left| \left( \int_0^x u(z) \mathrm{d}z \right) - y(x) \right|^2 \mathrm{d}x, \tag{15}$$

where $u'(x)$ is the first derivative of the function $y(x)$, and $\alpha$ is a regularization term that weights the first term, a penalty term, against the second term, the data fidelity term.

The total variation suppresses the noise without removing discontinuities in the derivative. The appeal of this approach is that a pillbox PSF has two finite discontinuities and this method ensures that they can be recovered and, additionally, that noise suppression is achievable. The main problem is the choice of the regularization parameter $\alpha$ as it affects the derivative produced.

## 5. EXPERIMENTAL RESULTS, FOCUSED AND DEFOCUSED SYSTEMS

### A. PSF Recovery Algorithm

Initially a knife-edge was set up on a lightbox so that it was angled with a slight offset to a row of pixels in the FPA. Its image was windowed ($51 \times 500$ pixels) as shown in Fig. 8. Individual ESFs along the edge therefore contained 51 samples from black to white. This width was sufficient even for defocused lens measurements.

The sampled ESFs were normalized to remove nonuniform illumination along the direction of the edge. Next the central brightness positions of the ESFs were estimated using a cubic fit and the ESFs aligned to these. This alignment resulted in the samples being displaced relative to each other. The superresolution edge was created by averaging the pixel intensities within subpixel bins to give a ten-times resolution improvement. Having obtained the mean ESF for a given distance, $f$-number, and knife-edge angle it was necessary to find the PSF. The methods examined were as follows:

(1) five-point numerical differentiation,
(2) regularized numerical differentiation using Chartrand's algorithm [24],
(3) regularized numerical differentiation using Chartrand's algorithm followed by a fit of the resulting PSF to a generalized Gaussian function,
(4) fitting the ESF to a sum of Fermi-Dirac functions [14],
(5) fitting the ESF to a defocused step assuming even illumination and a Gaussian PSF,
(6) fitting the ESF to a defocused step where the illumination is assumed to have a linear dependence on position and a Gaussian PSF,
(7) fitting the ESF to a defocused step assuming even illumination and a generalized Gaussian PSF,
(8) fitting the ESF to a defocused step where the illumination is assumed to have a linear dependence on position and a generalized Gaussian PSF.

In this section results for a 24 mm photographic lens fitted to a Basler A631fc color camera are presented when the lightbox was 0.725 m from the camera.

### B. Specific 1D Results

The results from the five-point numerical differentiation [item (1) above] in Fig. 9 show that although the ESF looks fairly smooth, the noise is swamping the underlying PSF, thus making this approach unusable without further processing.

When the measured ESF was fitted to a sum of Fermi–Dirac functions [item (4) above] as shown in Fig. 10, the ESF appeared to have a good fit; however, the PSF had neither symmetry nor a single peak. These are properties expected of a physical PSF.

### C. Regularized Numerical Differentiation

In order to determine the optimum regularization parameter $\alpha$, a series of simulations were performed. Both pillbox and Gaussian PSFs were used to defocus an ideal

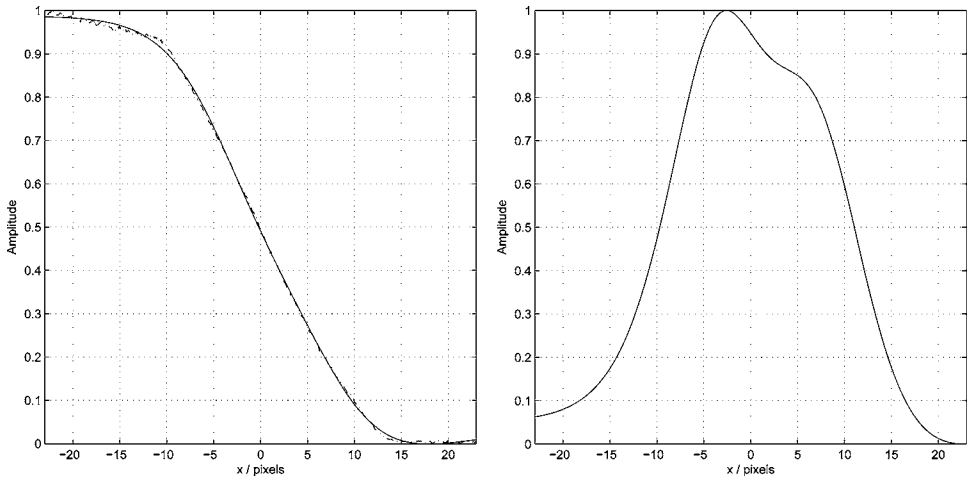


Fig. 10. Actual ESF (dashed curve) and Fermi–Dirac fitted ESF (solid curve) results for $f/2.8$, $z=0.725$ m, angle=0° (left), and PSF (right).

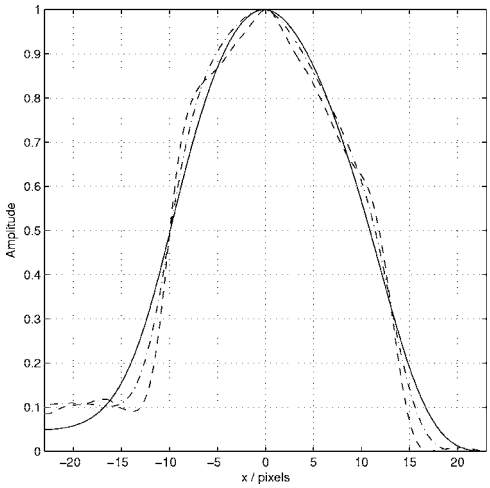


Fig. 11. Regularized numerical differentiation results (right) for $\alpha=10$ (dashed curve), $\alpha=100$ (dash–dotted), and $\alpha=1000$ (solid).

step. Three levels of noise were added with SNRs of 20 (high noise), 25, and 30 (low noise) dB, and then the ESF was differentiated using Chartrand's algorithm [24]. The (mean squared error) (MSE) was employed as a distance measure between the actual PSF and the result of the numerical differentiation. The value $\alpha=1000$ was optimum for the SNR=20 dB case, while $\alpha=100$ was optimum for 25 and 30 dB. These values were employed in the modeling of real ESFs. An example is shown in Fig. 11, where we have taken the low noise case because it illustrates a problem with the method in that it could not take into account nonuniform illumination and produced nonsymmetric PSFs.

The remaining fitting methods produced PSFs with less noise and better symmetry and so were processed further to give 2D results.

### D. Edge-Spread Function Fitting Experiments

The ESFs were fitted to the various functions for a range

**Table 1. MSE[a] Results for $f/2.8$ as a Function of Depth to Lightbox**

| | Depth to Lightbox, m | | | | |
|---|---|---|---|---|---|
| Method | 0.414 | 0.491 | 0.569 | 0.647 | 0.725 |
| Fermi–Dirac | 25.2 | 29.2 | 34.3 | 28.3 | 26.1 |
| Generalized Gaussian without I.C.[b] | 10.3 | 7.37 | 9.03 | 5.58 | 6.45 |
| Generalized Gaussian with I.C. | 7.91 | 5.92 | 7.95 | 4.99 | 6.01 |
| Gaussian without I.C. | 64.6 | 51.1 | 64.9 | 68.2 | 70.2 |
| Gaussian with I.C. | 47.6 | 43.4 | 55.0 | 51.1 | 48.5 |
| Pillbox without I.C. | 130.0 | 90.9 | 90.7 | 86.0 | 85.5 |
| Pillbox with I.C. | 102.0 | 70.3 | 72.4 | 70.8 | 68.3 |

[a]Mean squared error/$10^{-3}$.

[b]Illumination correction.

**Table 2. MSE[a] Results for All Three Apertures, from Best to Worst**

| Method | Average MSE /$10^{-3}$ |
|---|---|
| Generalized Gaussian with I.C.[b] | 5.04 |
| Generalized Gaussian without I.C. | 6.93 |
| Sum of three Fermi–Dirac functions | 26.7 |
| Gaussian with I.C. | 42.5 |
| Gaussian without I.C. | 56.7 |
| Pillbox with I.C. | 72.0 |
| Pillbox without I.C. | 97.6 |

[a]Mean squared error/$10^{-3}$.

[b]Illumination correction.

of distances. The results for aperture $f/2.8$ are displayed in Table 1. It shows the MSE of the fit as an average for all angles tested, which were −80 to +90° in 10° intervals. The plane in focus was at 0.414 m in front of the lens.

The results show that the error assuming a pillbox PSF decreases for increasing defocusing, which was expected from the diffraction-based optics theory in Section 3. The MSEs of the fits using generalized Gaussian, Gaussian, and pillbox models are lower when the nonuniform illumination was taken into account. The experiment was repeated for $f$-numbers of $f/4$ and $f/5.6$. In Table 2, the summarized results for all apertures show that the generalized Gaussian with illumination correction has resulted in the lowest MSE, thus giving the best fit to the data. The pillbox model produced the worst results with a MSE ~14 times greater than that of the generalized Gaussian. The MSE of the Gaussian fell almost halfway between the generalized Gaussian and the pillbox.

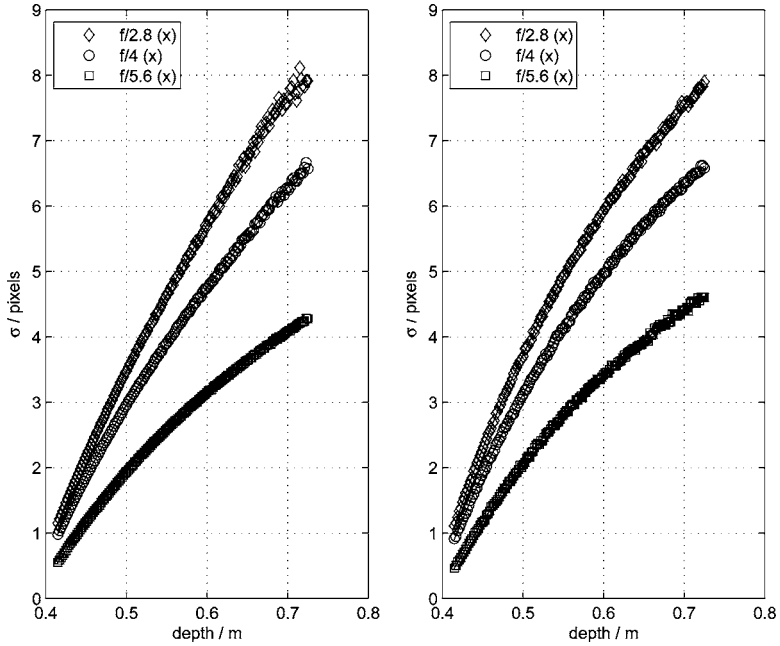


Fig. 12. Standard deviation against depth when fitting (left) a Gaussian PSF and (right) a generalized Gaussian PSF.

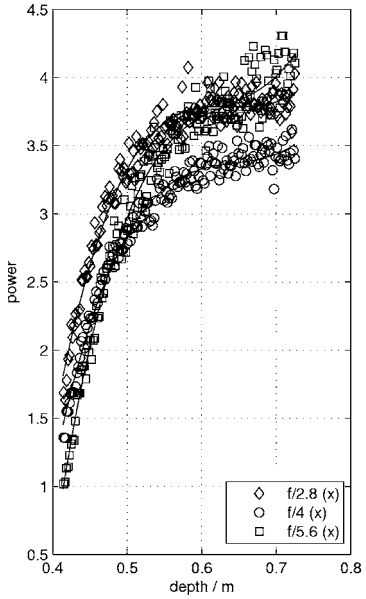


Fig. 13. Power of the generalized Gaussian against depth.

### E. Results Assuming Gaussian and Generalized Gaussian PSFs

Images of the knife-edge were obtained in 1 mm increments over a 30 cm depth range for angles of −80 to +90° in 10° increments. Each image gave a single mean ESF and that ESF was fitted assuming both Gaussian and generalized Gaussian PSFs as derived in Section 4. The PSFs were found to be very nearly circularly symmetric, and so the following results are given for the $x$ direction only. Figure 12 shows the standard deviation of both the Gaussian and generalized Gaussian as a function of distance for three different f-numbers tested. The plots appear to be smooth and increase monotonically, except for the Gaussian at the maximum distance tested for $f/2.8$. Being more robust with increasing depth, the generalized Gaussian is considered a better model for use with DFD [22].

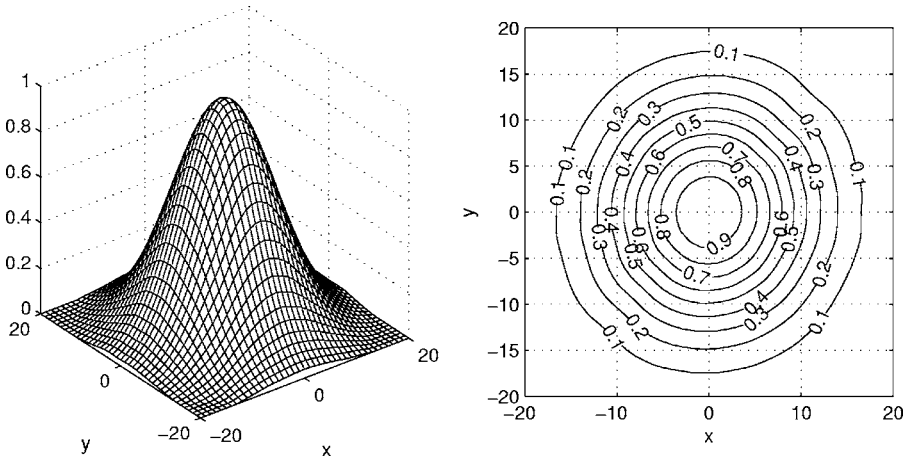


Fig. 14. Two-dimensional PSF assuming a Gaussian model for $z=0.725$ m and $f/2.8$, where $x$ and $y$ are in pixels.

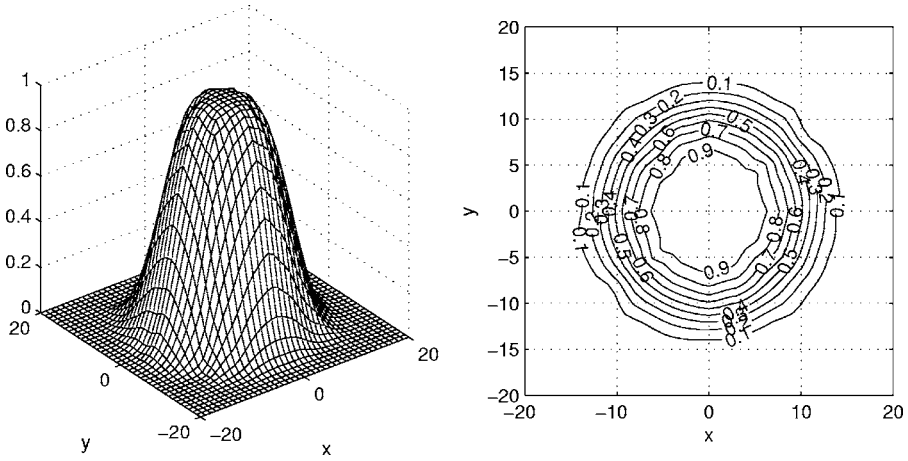


Fig. 15. Two-dimensional PSF assuming a generalized Gaussian model for $z=0.725$ m and $f/2.8$, where $x$ and $y$ are in pixels.

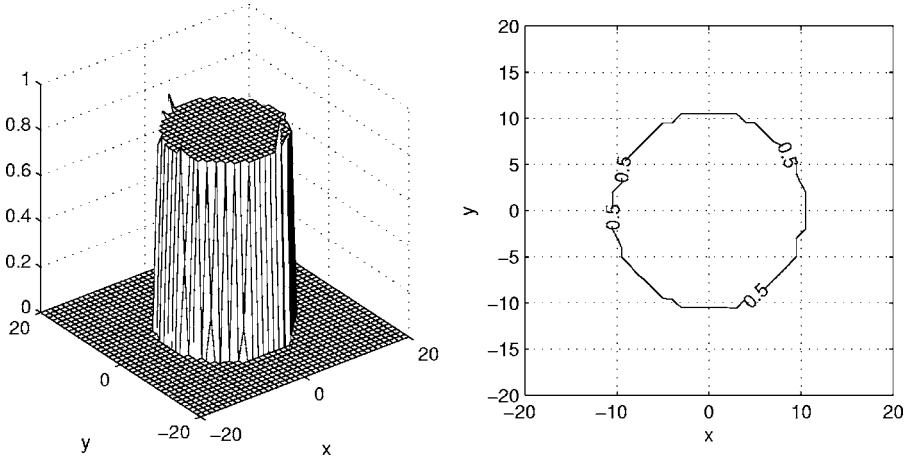


Fig. 16. Two-dimensional PSF assuming a pillbox model for $z=0.725$ m and $f/2.8$, where $x$ and $y$ are in pixels.

The generalized Gaussian PSF has two parameters, the standard deviation $\sigma$ and the power $p$. When the power as a function of depth was plotted it was found to be noisier than $\sigma$ as shown in Fig. 13.

### F. Two-Dimensional PSFs

Complete 2D PSFs are presented below assuming pillbox, Gaussian, and generalized Gaussian PSF models for two depths corresponding to the farthest and closest positions

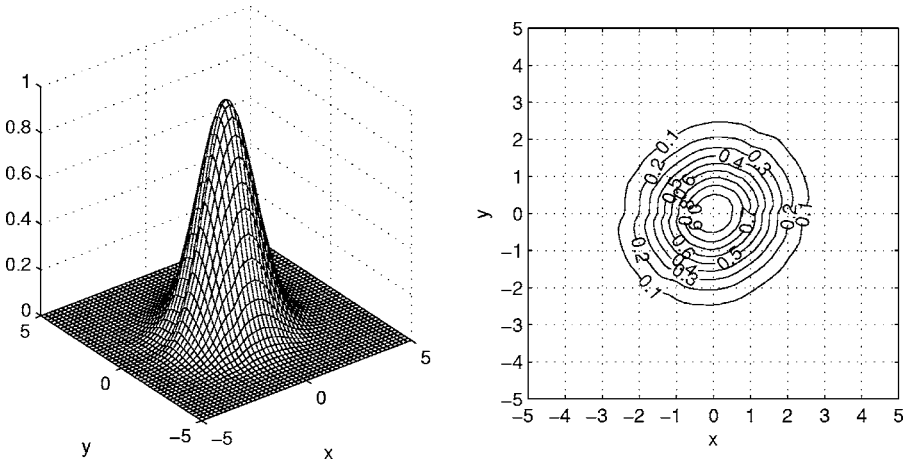


Fig. 17. Two-dimensional PSF assuming a Gaussian model for $z=0.414$ m and $f/2.8$, where $x$ and $y$ are in pixels.

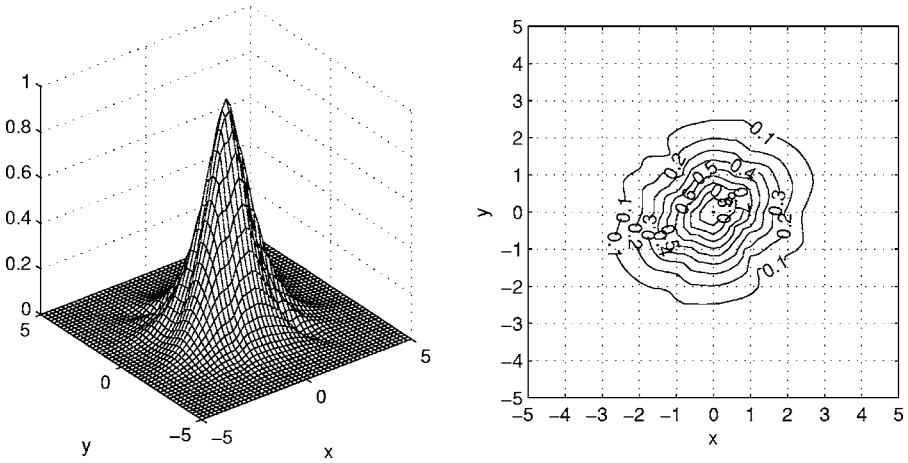


Fig. 18. Two-dimensional PSF assuming a generalized Gaussian model for $z=0.414$ m and $f/2.8$, where $x$ and $y$ are in pixels.

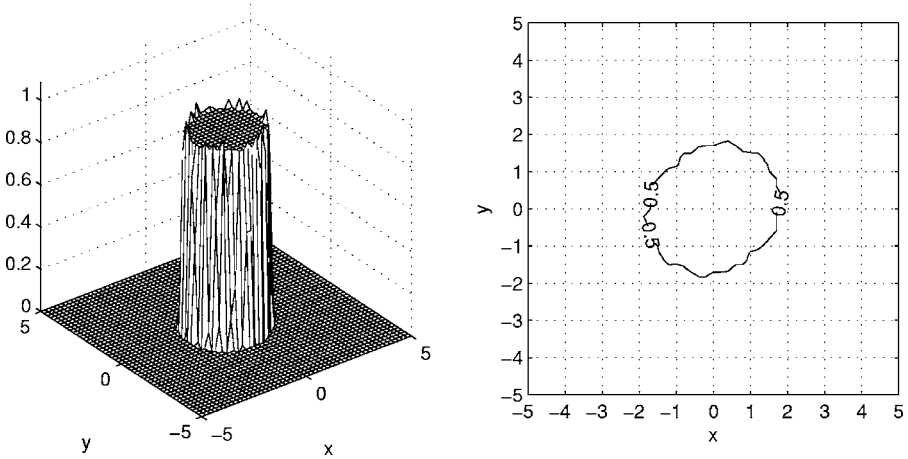


Fig. 19. Two-dimensional PSF assuming a pillbox model for $z=0.414$ m and $f/2.8$, where $x$ and $y$ are in pixels.

tested. The nonuniform illumination improvement was used. Figures 14–16 show the PSFs for a distance $z=0.725$ m between the camera and the lightbox for an aperture of $f/2.8$.

The Gaussian PSF model shown in Fig. 14 is for a defocused lens and is clearly circularly symmetric. The fit has resulted in a smooth contour plot. The generalized Gaussian PSF model shown in Fig. 15 appears to be a cross between the Gaussian and a pillbox. The fit has resulted in a contour plot that is less smooth than for the Gaussian, which is probably due to noise in the ESFs and increased complexity of the function because it has more

**Table 3. Average MSE/$10^{-3}$ for Each Method**

| | *f*-number | | |
|---|---|---|---|
| Method/Direction | 2.8 | 4 | 5.6 |
| Gaussian/ *x* direction | 31.7 | 21.9 | 23.3 |
| Gaussian/ *y* direction | 46.1 | 27.3 | 23.7 |
| Generalized Gaussian/ *x* direction | 2.20 | 1.67 | 1.42 |
| Generalized Gaussian/ *y* direction | 4.99 | 2.44 | 1.87 |

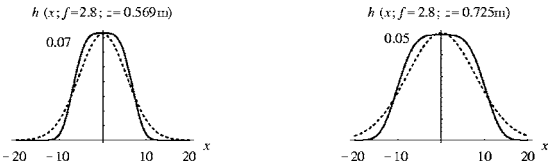


Fig. 20. Comparison between PSFs for the Gaussian (dashed curve) and generalized Gaussian (solid curve).

parameters than all the other models. The pillbox model, Fig. 16, has resulted in a reasonably circular PSF. Figures 17–19 show the PSFs for $z=0.414$ m, the in-focus case.

Note the change of $x$ and $y$ axis scales in Figs. 17–19. Now all three models have less circular symmetry and have a maximum spread at ~45° to the $x$ axis. The power of the generalized Gaussian is less than two, and so the function is more pointed than that for the Gaussian.

### G. Discussion

The goodness of fit of the generalized Gaussian PSF is exemplified by the results of Table 3. Where the nonuniform illumination model was employed, the fit was between 9 and 16 times better than for a Gaussian PSF.

The Gaussian PSF has a faster roll-off when the camera is very defocused compared to that using the generalized Gaussian because the power of the generalized Gaussian increases with defocus, making it more pillbox in shape, as highlighted in Fig. 20.

## 6. CONCLUSION

We have reported improvements to an easily performed superresolution, but averaged, PSF estimation method that enables it to be used for focused and defocused lenses and with noise generated within the camera. The method involved the initial accumulation of a superresolution ESF. Previously the calculation of the PSF from the ESF could give both noisy and distorted results.

Distortions were attributed to nonuniform illumination of the knife-edge test object. Where a model of the illumination could be incorporated into the computation of the PSF, symmetrical functions resulted.

Previously noise in the ESF was amplified when it was differentiated to form the PSF. We researched a regularized numerical differentiation that greatly reduced the noise. However, changes to the value of the regularization parameter chosen resulted in varying distortions of the PSF. The method was not constrained by any assumption of an underlying model of the ESF or PSF, but in practice, it was found to be outperformed by methods that did.

Several widely used models of the PSF were investigated including the pillbox and the Gaussian, together with the use of Fermi–Dirac fitting functions in both cases. A generalized Gaussian that incorporated pillbox, Gaussian, and a continuum of models in between through the choice of a parameter, was also used to model the PSF. The corresponding models for the ESF were derived from these as reported above. The results showed that the MSE of the fit using the generalized Gaussian performed best across the range of distances and *f*-numbers tested, and that it was 8 times better than the Gaussian model and 14 times better than the pillbox model. Pillbox and Gaussian models are often assumed in DFD work, and this research has shown that both are suboptimum. Finally, 1D PSFs for various knife-edge angles were combined to form 2D PSFs.

## REFERENCES

1. R. G. White and R. A. Schowengerdt, "Effect of point spread functions on precision step edge measurement," J. Opt. Soc. Am. A **11**, 2593–2603 (1994).
2. R. C. Staunton, "Edge operator error estimation incorporating measurements of CCD TV camera transfer function," IEE Proc. Vision Image Signal Process. **145**, 229–235 (1998).
3. R. C. Staunton, "Detected edge evaluation using measured acquisition system parameters," Pattern Recogn. Lett. **26**, 1609–1619 (2005).
4. A. Pentland, "A new sense for depth of field," IEEE Trans. Pattern Anal. Mach. Intell. **9**, 523–531 (1987).
5. M. Subbarao and N. Gurumoorthy, "Depth recovery from blurred edges," in *Proceedings of IEEE Conference on Computer Vision and Pattern Recognition* (IEEE, 1988), pp. 498–503.
6. J. Ens and P. Lawrence, "An investigation of methods for determining depth from focus," IEEE Trans. Pattern Anal. Mach. Intell. **15**, 97–108 (1993).
7. M. Subbarao and G. Surya, "Depth from defocus: a spatial domain approach," Int. J. Comput. Vis. **13**, 271–294 (1994).
8. A. N. Rajagopalan and S. Chaudhuri, "A variational approach to recovering depth from defocused images," IEEE Trans. Pattern Anal. Mach. Intell. **19**, 1158–1164 (1997).
9. M. Watanabe and S. Nayar, "Rational Filters for Passive Depth from Defocus," Int. J. Comput. Vis. **27**, 203–225 (1998).
10. Li-Ma and R. C. Staunton, "Integration of multiresolution image segmentation and neural networks for object depth recovery," Pattern Recogn. **38**, 985–996 (2005).
11. P. Favaro and S. Soatto, "A geometric approach to shape from defocus," IEEE Trans. Pattern Anal. Mach. Intell. **27**, 406–417 (2005).
12. D. K. Schroder, *Advanced MOS Devices* (Addison Wesley, 1987).
13. S. E. Reichenbach, S. K. Park, and R. Narayanswamy, "Characterizing digital image acquisition devices," Opt. Eng. (Bellingham) **30**, 170–177 (1991).
14. A. P. Tzannes and J. M. Mooney, "Measurement of the modulation transfer function of infrared cameras," Opt. Eng. (Bellingham) **34**, 1808–1817 (1995).
15. D. Kavaldjiev and Z. Ninkov, "Influence of nonuniform charge-coupled device pixel response on aperture photometry," Opt. Eng. (Bellingham) **40**, 162–169 (2001).
16. G. Boreman and E. L. Dereniak, "Method for measuring modulation transfer-function of charge-coupled-devices using laser speckle," Opt. Eng. (Bellingham) **25**, 148–150 (1986).
17. J. C. Feltz and M. A. Karim, "Modulation transfer-function of charge-coupled-devices," Appl. Opt. **29**, 717–722 (1990).

18. M. Marchywka and D. G. Socker, "Modulation transfer-function measurement technique for small-pixel detectors," Appl. Opt. **31**, 7198–7213 (1992).
19. A. Daniels, G. D. Boreman, and A. D. Ducharme, "Random transparency targets for modulation transfer-function measurement in the visible and infrared regions," Opt. Eng. (Bellingham) **34**, 860–868 (1995).
20. A. Rosenfeld and A. C. Kak, *Digital Picture Processing* (Academic, 1982).
21. T. J. Schultz, "Multiframe image restoration," in *Handbook of Image and Video Processing*, A. Bovic, ed. (Academic, 2000), pp. 175–189.
22. C. D. Claxton, "Colour depth-from-defocus incorporating experimental point spread function measurements," Ph.D. dissertation (University of Warwick, Coventry, U.K., 2007).
23. A. Tarantola, *Inverse Problem Theory: Methods for Data Fitting and Model Parameter Estimation* (Elsevier, 1987).
24. R. Chartrand, "Numerical differentiation of noisy, nonsmooth data," http://math.lanl.gov/Research/Publications/Docs/chartrand-2005-numerical.pdf.